A Cost-Efficient Hybrid UHF RFID and Odometry-Based Mobile Robot Self-Localization Technique With Centimeter Precision

Christoph Kammel [ID], Tobias Kögel [ID], *Graduate Student Member, IEEE*, Matthias Gareis [ID], and Martin Vossiek [ID], *Fellow, IEEE*

Abstract—This paper presents an indoor localization approach that determines the absolute position of a mobile robot platform with centimeter precision by fusing RFID localization results based on cost-effective, standard passive UHF RFID technology with the robot's odometry data. The mobile robot platform is equipped with a multistatic UHF RFID interrogation system, and several RFID tags are arbitrarily placed within the localization environment, serving as landmarks. The RFID localization concept is based on phase evaluations. To overcome the problem of ambiguous position estimations due to the 2π-phase ambiguity of the RFID signal phase and mitigate the linearization problem of the nonlinear system, a novel algorithm based on an iterative multihypothesis Kalman filter is introduced. A realistic simulation setup is developed to validate the proposed filter algorithm. By tracking a UHF RFID-equipped mobile robot platform in a real-world office environment, the proposed approach is also practically tested in terms of real-time capability, everyday suitability, and multipath resistance. Given that centimeter precision is only achieved in environments with weak multipath propagation, the RFID localization results are fused with odometry data provided by the robot. This effectively compensates for offset and drift in the odometry sensor, achieving a root-mean-square localization error of 2.7 cm.

Index Terms—Autonomous robot, global localization, indoor positioning, Industry 4.0, Internet of Things, iterative unscented Kalman filter, MIMO, multihypothesis Kalman filtering, phase-based localization, radio frequency identification, RFID robot, self-localization, synthetic aperture, UHF RFID.

I. INTRODUCTION

SELF-LOCALIZATION has become an essential technology, especially with the deployment of autonomous robots in a variety of applications. In this paper, we focus on the self-localization of autonomous UHF RFID-equipped robots, which have emerged as a powerful platform in the digital transformation of industry (often called the Fourth Industrial Revolution, 4IR, or Industry 4.0), with the first commercial robots already available for purchase [1].

A. UHF RFID and Self Localization

The use of UHF RFID has become widespread since its introduction in the EPCglobal Class-1 Gen2 standard [2], with an estimated market size of USD 10.7 billion in 2021 and a compound annual growth rate of 10.2% [3]. Its prevalence originates from the fact that it offers an increased reading range and higher data rate compared with low-frequency and high-frequency RFID standards. Since passive tags do not require any maintenance and are very inexpensive to manufacture, this technology is particularly well suited to economically implement the Internet of Things in environments with large quantities of items [4]. Every tag provides a virtual fingerprint in the form of a unique Electronic Product Code (EPC) that is physically applied to the actual item. While this technology has been used primarily for identification in the past, a growing body of literature is now recognizing its great potential in the fields of indoor tracking, navigation, and positioning [5]–[7].

Autonomous robots equipped with UHF RFID readers are able to fully embrace these possibilities. By freely navigating through an unknown environment while locating tagged goods from a distance of up to 10 meters, these robots provide a cost-effective solution for autonomous stocktaking in smart warehouses [8], [9], big storage facilities, and even libraries [10], thus reducing the costs of inventory discrepancies and providing online stock data.

The mobile robot platform presented in [11], which is also used in this paper, is capable of locating tagged goods with a root-mean-square error (RMSE) of 1.45 cm. To achieve this remarkable grade of localization accuracy, it is essential to know the position of the mobile robot precisely throughout the entire recording. Typically, proprioceptive data (e.g., odometry data) are retrieved for this purpose. Unfortunately, this is not sufficient for long trajectories, as error accumulates over time when a dead reckoning approach is applied [12]. Therefore, exteroceptive sensor data are used to oppose the characteristic drift of the estimated trajectory by data fusion. Obtaining this data in indoor environments often requires expensive hardware [12], such as cameras [13], sonars [14], and laser range finders [15].

Autonomous robot platforms are often already equipped with UHF RFID readers for inventory purposes, which can also be utilized for self-localization. Tags that have been distributed around the trajectory of the robot can then serve

as landmarks with known positions. Since this approach completely eliminates the need for additional exteroceptive sensors, it greatly reduces the overall costs and therefore considerably increases the economic efficiency of autonomous inventory robots, accelerating the emergence of Industry 4.0.

B. State of the Art

UHF RFID-based localization systems can be divided into three categories: systems that evaluate tag readability [16], received signal strength (RSSI) [17], or the phase information of the received tag responses. Systems based on readability solely utilize the information about which tag is responding at the current robot position and are thus the most basic localization technique. The RSSI-based approach also considers the amplitude of the tag signal for position estimation. However, both metrics are highly dependent on several factors, including chip sensitivity, the tagged item material, and the tag model. Additionally, these metrics often require complex calibration procedures that are very sensitive to environmental changes [18]. A phase-based approach typically outperforms the above methods because of its higher sensitivity and robustness when confronted with multipath propagation phenomena, as these phenomena especially occur in indoor environments [19].

In [5] and [19], a detailed overview of the most recent publications in the field of phase-based UHF RFID self-localization algorithms is presented. Among other publications, a precise localization system based on a data fusion approach using wheel encoders and a UHF RFID system with custom tags is presented, which achieves an accuracy of approximately 4 cm [20], [21]. Unfortunately, custom tags are rather impractical because of the additional costs incurred when used in large quantities. In [18] and [22], commercial tags were placed on the ceiling and floor, necessitating the installation of additional upward- and downward-pointing antennas, whereas typical inventory systems require side-facing antennas. Moreover, floor-mounted tags can be easily destroyed by roaming vehicles and humans, whereas ceiling-mounted tags may be inaccessible in tall buildings, such as warehouses. Additionally, the presented publications do not utilize the full 360° phase information and therefore waste a lot of localization potential.

By contrast, this paper presents a localization system based on a multiple-input and multiple-output (MIMO) 360° cost-effective iterative multihypothesis unscented Kalman filter (IMUKF), which evaluates the phase data of commercial tags attached to the surrounding walls, enabling the usage of side-facing antennas, which are typically mounted on inventory robots [23]. This paper offers exclusive insight into the performance of the standalone RFID localization approach in a high-multipath real-world office scenario, allowing for a deeper understanding of the opportunities and limitations of this technology. To sustain the high-precision localization of the mobile robot platform, even in harsh environments, the IMUKF is used in a hybrid odometry RFID data fusion approach, compensating for the drift caused by erroneous odometry data. This leads to highly accurate localization

results without incurring additional hardware costs from expensive exteroceptive sensors.

The remaining parts of this paper are organized as follows: Section II discusses the underlying theory of the hybrid localization principle, including a closer look at the UHF RFID-based robot localization and the data fusion approach using proprioceptive odometry data, followed by a detailed description of the system architecture in Section III. An evaluation of the IMUKF algorithm is provided in Section IV using a simulation setup with close approximation to the real measurement scenario. In Section V, the simulated RFID-only localization algorithm and the novel hybrid data fusion approach are tested with actual measurement data in a demanding use case scenario. Finally, the results are summarized and future research directions are discussed in Section VI.

II. Hybrid Robot Localization Based on UHF RFID Landmarks and Proprioceptive Odometry Data

Both a UHF RFID system and odometry data acquired by means of wheel encoders are available for localizing the mobile robot platform. When the robot's starting position and orientation are known, the odometry sensors are able to momentarily provide highly accurate results exceeding the performance of the UHF RFID system by several orders of magnitude. However, given that odometry sensors only measure changes in position and orientation, even minimal deviations in the detected robot pose, which occur due to slip during turning maneuvers or when crossing door thresholds, lead to considerable localization errors of up to several meters when measuring over long periods of time. These deviations can only be compensated by absolute position measurements, such as the exteroceptive localization results of the UHF RFID system. Thus, we present a hybrid approach that uses both exteroceptive RFID data and proprioceptive odometry data to maintain the high accuracy of odometry sensors over long localization periods. In the following section, we first describe the UHF RFID-based localization principle before considering the data fusion using odometry measurements in more detail.

A. Localization Scenario

Fig. 1 shows a typical robot localization scenario in which a mobile robot platform is equipped with N antennas, shown as blue points at the positions $\vec{r}_{\text{ant},n}$, moving along a trajectory of unknown position $\vec{r}_{t_i}$ at the time $t = t_i$. Furthermore, K tags are mounted in our global localization environment at known positions $\vec{r}_{\text{tag},k}$, which serve as landmarks. We define the tag-to-antenna distance as

$$d_{\text{ant-tag},n/mk} = \| \vec{r}_{\text{ant},n/m} - \vec{r}_{\text{tag},k} \|_2, \tag{1}$$

for the n/m-th receiving (RX) and transmitting (TX) antennas and the k-th tag, where $\|\cdot\|_2$ defines the Euclidean norm, with $n, m \in N$ and $n \neq m$ for our bistatic scenario. Therefore, the received signal for a time stamp $t = t_i$ is given as

$$\vec{x}_{t_i}(\vec{r}_{\text{tag},k}) = \vec{A}_{t_i}(\vec{r}_{\text{tag},k}) \vec{a}_{t_i}(\vec{r}_{\text{tag},k})$$
$$= \vec{A}_{t_i}(\vec{r}_{\text{Tag},k}) \left[e^{-j\varphi_{k,1}}, e^{-j\varphi_{k,2}}, \ldots, e^{-j\varphi_{k,U}} \right]^{\mathsf{T}}, \tag{2}$$
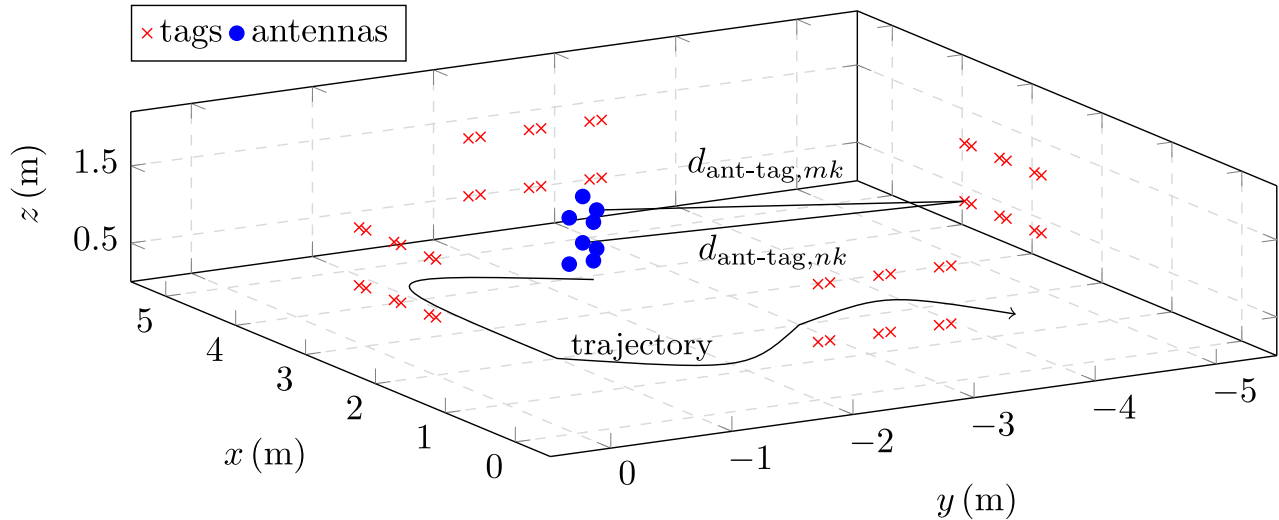
Fig. 1. Localization scenario: N antennas, shown as blue dots, move along a trajectory and receive responses from K tags located at the red markers.

where $\vec{A}_{t_i}(\vec{r}_{\text{tag},k})$ is the amplitude of the k-th vector and is set to one, and $\varphi_{k,u}$ is the detected signal phase of the k-th tag using the u-th signal path. The phase steering vector $\vec{a}_{t_i}(\vec{r}_{\text{tag},k})$ contains the signal phases of all U possible signal paths for a time $t = t_i$, which are all possible antenna-to-tag and tag-to-antenna combinations according to the MIMO principle, as described in [11]. Finally, the signal phase is given by

$$\varphi_{k,u} = \left(2\pi \frac{d_{\text{ant-tag},nk} + d_{\text{ant-tag},mk}}{\lambda_{\text{c}}} + \varphi_{\text{offset},u}\right) \mod 2\pi, \quad (3)$$

where the phase offset $\varphi_{\text{offset},u}$ of the u-th MIMO path is caused by the cables, the switch matrix, the antennas, and the listener.

This offset is assumed to be independent of the tag index k, as only small variations in the phase shift caused by different tags have been observed in the course of several measurements. Moreover, the dependence of the phase offset on the propagation angle due to the angle-dependent radiation patterns of the antennas and tags can be neglected. This assumption is valid, given that, first, the radiation pattern of the meandered dipole tag antennas is comparable to an ideal dipole [24], [25], leading to concentrically propagated waves [26]. Second, the maximum phase change within the main lobe of the robot-mounted antennas is 3°, as found in simulations. This deviation is negligible compared to other noise effects, such as multipath. Finally, no significant detuning effect was observed over several weeks, indicating the phase offset to be constant over time. Hence, $\varphi_{\text{offset},u}$ depends only on the MIMO channel index u and can therefore be compensated for by a low-effort calibration, as described in Section V-A.

B. Localization Principle

The proposed algorithm solves the global localization problem in real time by using a motion model and phase measurements according to (2) at a known time stamp $t = t_i$ to predict a new robot position.

This algorithm, based on a Bayes filter, is capable of solving 2π phase ambiguity (which typically results in ambiguous robot position estimation) and is implemented in the form of an IMUKF. The process of robot localization starts by finding the rough initial robot position. This position is obtained using the standard synthetic-aperture radar (SAR) algorithm, as presented in [11], by creating a set of hypothetical phases $\tilde{\varphi}_{k,l,u}$ according to (3) for an assigned grid on the search space at L hypothetical robot positions $\vec{r}_{\text{hyp},l}$. Furthermore, the steering vector for this set of phases is given by

$$\vec{a}_{t_i}(\vec{r}_{\text{hyp},l}) = \left[e^{-j\tilde{\varphi}_{k,l,1}}, e^{-j\tilde{\varphi}_{k,l,2}}, \ldots, e^{-j\tilde{\varphi}_{k,l,U}}\right]^{\text{T}}. \quad (4)$$

Finding the maximum value of the beamformer output power by evaluating the first received I_{init} signals leads to the estimated starting position of the robot according to $\vec{\tilde{r}}_{\text{start}} = \text{argmax}(p(\vec{a}_{t_i}(\vec{r}_{\text{hyp},l})))$, with

$$p(\vec{a}_{t_i}(\vec{r}_{\text{hyp},l})) = \frac{1}{(t_{I_{\text{init}}} - t_0)U}$$
$$\cdot \left| \sum_{i=0}^{I_{\text{init}}} \sum_{k=0}^{K_{\text{det}}} \vec{a}_{t_i}(\vec{r}_{\text{hyp},l})^{\text{H}} \vec{x}_{t_i}(\vec{r}_{\text{Tag},k}) \right|^2, \quad (5)$$

and the number of detected tags K_{det}. In contrast to the SAR algorithm proposed in [11], the robot is not moving; thus, the spatial sampling theorem is not satisfied. Hence, the robot position found is likely not the correct robot position. This is why multiple weighted unscented Kalman filters (UKFs) are initialized at the Y most likely robot starting positions to track the movement of the robot while always taking incoming phase measurements into account and updating filter weights. The positional ambiguity is then solved by removing all filters with low weights until the most likely UKF remains, pointing to the robot's real position. If the uncertainty of the filter's position estimation strongly increases, a set of new UKFs are

initialized around the last actual robot position to remove the filter uncertainty caused by 2π phase ambiguity and noise effects, such as multipath or phase noise.

C. Bayes Filter Algorithm

Before the filter equations are given for the real-time global localization problem, the basic Bayes filter will be described briefly.

The predicted position and velocity of the robot at the time $t = t_i$ result from the previously measured values $\vec{x}_{t_0:t_{i-1}}$ according to

$$\overline{\mathrm{bel}}(\vec{r}_{t_i}) = p(\vec{r}_{t_i} | \vec{x}_{t_0:t_{i-1}}), \tag{6}$$

where $\vec{r}_{t_i} = [x_{\mathrm{robot}}, y_{\mathrm{robot}}, v_{\mathrm{x,robot}}, v_{\mathrm{y,robot}}]^{\mathsf{T}}$ is the state vector describing the position $[x_{\mathrm{robot}}, y_{\mathrm{robot}}]^{\mathsf{T}}$ and velocity $[v_{\mathrm{x,robot}}, v_{\mathrm{y,robot}}]^{\mathsf{T}}$ of the robot, and $\vec{x}_{t_0:t_{i-1}}$ is the phase measurement vector from the time t_0 to t_{i-1} [27]. The uncertainty of the predicted state vector is corrected in the update step, using the latest phase measurements $p(\vec{x}_{t_i} | \vec{r}_{t_i})$ according to

$$\mathrm{bel}(\vec{r}_{t_i}) = \eta \cdot p(\vec{x}_{t_i} | \vec{r}_{t_i}) \cdot \overline{\mathrm{bel}}(\vec{r}_{t_i}), \tag{7}$$

where η is a normalization factor to meet the requirements of a probability density function. The maximum of the resulting function is the best estimate of the robot's state vector [28].

D. Iterative Multihypothesis UKF

In the following sections, we first explain the prediction and update step of the UKF — based on the fundamentals of Kalman filtering and the unscented transformation [28]–[32]. Given the improved approximation of the nonlinear system equations and the resulting lower risk of filter divergence, we subsequently extend upon this step with the theoretical underpinnings of the iterative UKF (IUKF). Finally, we derive a multihypothesis approach to solve the 2π phase ambiguity of the position estimate.

1) Unscented Kalman Filter:

Prediction: Based on the state transition function f, the new state vector $\vec{r}_{\mathrm{rv},t_i}$, defined here as a random vector, is predicted from the previously estimated state vector of the last time stamp by adding normally distributed noise $\vec{v}_{t_{i-1}}$ according to

$$\vec{r}_{\mathrm{rv},t_i} = f(\vec{r}_{\mathrm{rv},t_{i-1}}) + \vec{v}_{t_{i-1}}, \tag{8}$$

where t_i is the current time stamp, and the state transition function is defined as

$$f(\vec{r}_{\mathrm{rv},t_{i-1}}) = \begin{pmatrix} 1 & 0 & t_i - t_{i-1} & 0 \\ 0 & 1 & 0 & t_i - t_{i-1} \\ 0 & 0 & 1 & 0 \\ 0 & 0 & 0 & 1 \end{pmatrix} \vec{r}_{\mathrm{rv},t_{i-1}}. \tag{9}$$

In the UKF algorithm, this is realized by creating $2l+1$ sigma points $\mathcal{X}_{t_{i-1}}^s$, as described in [28], from the last estimated state vector $\vec{r}_{\mathrm{rv},t_{i-1}}$, with $s = 0, \ldots, 2l$ and l being the dimensionality of the state vector. Then, these are transformed to the sigma points of the prediction according to

$$\mathcal{Y}_{t_i}^s = f(\mathcal{X}_{t_{i-1}}^s). \tag{10}$$

using

$$\vec{\tilde{r}}_{t_i} = \sum_{s=0}^{2l} w_{\mathrm{m},t_i}^s \mathcal{Y}_{t_i}^s \tag{11}$$

and

$$\tilde{\mathbf{P}}_{t_i} = \sum_{s=0}^{2l} w_{\mathrm{c},t_i}^s [\mathcal{Y}_{t_i}^s - \vec{\tilde{r}}_{t_i}][\mathcal{Y}_{t_i}^s - \vec{\tilde{r}}_{t_i}]^{\mathsf{T}} + \mathbf{Q}_{t_i}, \tag{12}$$

with the weights w_{m,t_i}^s and w_{c,t_i}^s defined in [28]. The mean $\vec{\tilde{r}}_{t_i}$ (the new predicted position and velocity of the robot) and the covariance $\tilde{\mathbf{P}}_{t_i}$ (describing the uncertainty of the prediction) of the predicted state vector $\vec{\tilde{r}}_{\mathrm{rv},t_i}$ are calculated. The term $\mathbf{Q}_{t_i}$ is added to express the uncertainty caused by using a non-ideal motion model to predict the new robot position and velocity.

Update: As the update step is performed in the measurement space, the update of the robot's predicted state vector begins with the transition of the vector into the measurement state using the state transition function h. The expected measurement vector is therefore given by

$$\vec{\tilde{x}}_{\mathrm{rv},t_i} = h(\vec{\tilde{r}}_{\mathrm{rv},t_i}) + \vec{w}_{t_i}, \tag{13}$$

where $\vec{w}_{t_i}$ is a normally distributed vector representing the noise of the measurement. The state transition function h applies (3) to obtain the expected phase value of the u-th MIMO channel, given the predicted state vector $\vec{\tilde{r}}_{\mathrm{rv},t_i}$. In the UKF algorithm, this transition is accomplished by transforming the predicted sigma points $\mathcal{Y}_{t_i}^s$ to the measurement space according to

$$\mathcal{Z}_{t_i}^s = h(\mathcal{Y}_{t_i}^s). \tag{14}$$

Again, the mean $\vec{\tilde{x}}_{t_i}$ and covariance $\tilde{\mathbf{P}}_{\tilde{x}\tilde{x},t_i}$ of the expected measurement vector $\vec{\tilde{x}}_{\mathrm{rv},t_i}$ are calculated according to

$$\vec{\tilde{x}}_{t_i} = \sum_{s=0}^{2l} w_{\mathrm{m},t_i}^s \mathcal{Z}_{t_i}^s \tag{15}$$

and

$$\tilde{\mathbf{P}}_{\tilde{x}\tilde{x},t_i} = \sum_{s=0}^{2l} w_{\mathrm{c},t_i}^s [\mathcal{Z}_{t_i}^s - \vec{\tilde{x}}_{t_i}][\mathcal{Z}_{t_i}^s - \vec{\tilde{x}}_{t_i}]^{\mathsf{T}} + \mathbf{R}_{t_i}, \tag{16}$$

where $\mathbf{R}_{t_i}$ describes the uncertainty of the vector $\vec{w}_{t_i}$ in the form of a covariance matrix, which takes into account the noise of the measurement.

With these parameters, the cross-covariance matrix $\tilde{\mathbf{P}}_{\tilde{r}\tilde{x},t_i}$ is calculated according to

$$\tilde{\mathbf{P}}_{\tilde{r}\tilde{x},t_i} = \sum_{s=0}^{2l} w_{\mathrm{c},t_i}^s [\mathcal{Y}_{t_i}^s - \vec{\tilde{r}}_{t_i}][\mathcal{Z}_{t_i}^s - \vec{\tilde{x}}_{t_i}]^{\mathsf{T}}, \tag{17}$$

which enables the calculation of the Kalman gain, given as

$$\vec{K}_{t_i} = \tilde{\mathbf{P}}_{\tilde{r}\tilde{x},t_i} \tilde{\mathbf{P}}_{\tilde{x}\tilde{x},t_i}^{-1}. \tag{18}$$

Then, the residuum of the prediction and the measurement

$$\vec{y}_{\mathrm{res},t_i} = [\vec{x}_{t_i} - \vec{\tilde{x}}_{t_i}] \tag{19}$$

with the measurement vector $\vec{x}_{t_i}$ of time stamp t_i is multiplied by the Kalman gain. The result is a correction vector, which takes into account the noise effects of the prediction and the measurement. Adding the correction vector to the first predicted state leads to the mean $\vec{r}_{t_i}$ of the estimated state vector $\vec{r}_{\text{rv},t_i}$ according to

$$\vec{r}_{t_i} = \vec{r}_{t_i} + \vec{K}_{t_i} \vec{y}_{\text{res},t_i}. \tag{20}$$

The uncertainty of this estimated state is expressed by the covariance matrix $\hat{\mathbf{P}}_{t_i}$, given by

$$\hat{\mathbf{P}}_{t_i} = \tilde{\mathbf{P}}_{t_i} - \vec{K}_{t_i} \tilde{\mathbf{P}}_{\tilde{x}\tilde{x},t_i} \vec{K}_{t_i}^{\mathsf{T}}, \tag{21}$$

which is the difference of the covariance matrix from the prediction step $\tilde{\mathbf{P}}_{t_i}$ and the Kalman gain-weighted covariance matrix of the measurement.

As the proposed filter evaluates only one phase measurement at a time, the residuum $\vec{y}_{\text{res},t_i}$ can also be represented by a scalar y_{res,t_i} with variance σ^2_{UKF}.

2) Solving Multimodal Probability Densities (The Multihypothesis UKF): The 2π ambiguity of the phase leads to a multimodal probability density, which cannot be solved by a UKF that is based on a unimodal noise probability density. Thus, an incorrect robot starting position cannot be avoided without further signal processing techniques. As mentioned previously, we therefore initiate Y UKFs at the likely starting positions and weigh them according to the residuum of the prediction and measurement from above.

Every initialized UKF filter tries to track the robot when it starts moving by using the UKF algorithm's predict and update step. The filter with the highest weight, which for the c-th filter is given by

$$\gamma_{t_i,c} = \gamma_{t_{i-1},c} \eta_{\text{ukf}} e^{-\frac{y^2_{\text{res},t_i,c}}{2\sigma^2_{\text{UKF}}}}, \tag{22}$$

tracks the real robot position, where η_{ukf} is the speed of the filter to converge, and σ^2_{UKF} is the variance of the residuum $y_{\text{res},t_i,c}$ [20]. Both η_{ukf} and σ^2_{UKF} are empirically optimized for the best possible filter behavior using several simulations. When the weights are lower than the minimum threshold, the corresponding filters are deleted until a final filter remains and tracks the correct robot position.

To achieve even more robustness against noise effects, the factors $\gamma_{t_i,c}/\gamma_{t_{i-1},c}$ are stored and averaged over a set period of time. If the average falls below a given limit and the number of remaining filters is lower than $N_{\text{UKF,min}}$, a post-initialization process begins, and X new filters are initialized around the last known robot's position.

3) Improving the Localization Accuracy Due to Non-Linearities (The Iterative UKF): The UKF approximates the system transfer function by third-order Taylor series linearization [33]; thus, errors occur due to the 2π ambiguity. This can lead to a situation where the filter diverges [34], but the risk of divergence can be reduced by executing the filter equations iteratively. In this scenario, a phase measurement at a time $t = t_i$ will be evaluated until new phase data arrive at the filter input. A pause between two phase measurements is common according to the EPCglobal GEN-2 Standard [2]. This

approach still meets the requirement of real-time capability and increases localization accuracy by reducing linearization error.

Based on the basics of iterative Kalman filtering [35]–[40], the algorithm developed herein carries out these steps:

1. The last estimated state vector given as $\vec{r}_{\text{rv},t_i,g-1}$ becomes the new prediction, and the sigma points $\mathcal{X}^s_{t_i,g}$ are calculated, where $g - 1$ with $g \in \mathbb{N}$ is the last step of the iteration. After building the weights, the mean (i.e., the predicted position and velocity) $\vec{r}_{t_i,g}$ is given.

2. The transition of the sigma points into the measurement state according to (14) gives $\mathcal{Z}^s_{t_i,g}$. The weighting according to (15) calculates the expected measurement vector $\vec{x}_{t_i,g}$ of the g-th iteration.

3. Finally, the calculation of the covariances $\tilde{\mathbf{P}}_{\tilde{x}\tilde{x},t_i,g}$ and $\tilde{\mathbf{P}}_{\tilde{r}\tilde{x},t_i,g}$ and the Kalman gain $\vec{K}_{t_i,g}$ according to (16), (17), and (18) lead to the new estimated state vector $\vec{r}_{\text{rv},t_i,g}$ with its mean $\vec{r}_{t_i,g}$ and covariance matrix $\hat{\mathbf{P}}_{t_i,g}$. The corresponding equations are as follows:

$$\vec{r}_{t_i,g} = \vec{r}_{t_i,g} + \epsilon^{g-1} \vec{K}_{t_i,g} \left[\vec{x}_{t_i} - \vec{x}_{t_i,g} \right] \tag{23}$$

and

$$\hat{\mathbf{P}}_{t_i,g} = \hat{\mathbf{P}}_{t_i,g-1} - \vec{K}_{t_i,g} \tilde{\mathbf{P}}_{\tilde{x}\tilde{x},t_i,g} \vec{K}_{t_i,g}^{\mathsf{T}}, \tag{24}$$

where $\hat{\mathbf{P}}_{t_i,g-1}$ is the covariance matrix of the last estimation, and ϵ is a scaling factor with $0 < \epsilon < 1$ that is empirically optimized for best filter performance using several simulations.

These steps are repeated for any number of G iterations with $g \leq G$ until new phase data arrive at the UHF RFID listener.

E. Data Fusion Approach Using UHF RFID-Based Localization Results and Odometry Data

The proposed data fusion approach combines odometry data and the results of the UHF RFID-based localization algorithm described above to accurately estimate the position of the mobile robot platform, even for long measurement periods. For this purpose, the exteroceptive localization results are used to compensate for an initial position and orientation error in the proprioceptive data and for odometry drift during the measurement. To determine the current odometry shifts we minimized the distance between the robot position estimated by RFID measurement data $\hat{\vec{r}}_{t_i}$ and the corrected odometry data according to

$$(\Delta x, \Delta y, \Delta \phi)$$
$$= \operatorname{argmin} \left[\sum_i \left| \hat{\vec{r}}_{t_i} - \mathbf{A}(-\Delta\phi) \vec{r}_{\text{odo},t_i} - (\Delta x, \Delta y)^{\mathsf{T}} \right| \right], \tag{25}$$

with the odometry position shifting in the x-direction and the y-direction $(\Delta x, \Delta y)$, the orientation error $\Delta\phi$, the erroneous odometry position $\vec{r}_{\text{odo},t_i}$, and the rotation matrix $\mathbf{A}(-\Delta\phi)$ rotating $\vec{r}_{\text{odo},t_i}$ by the angle $-\Delta\phi$ around the z-axis.

To estimate the current antenna positions, the RFID-based localization algorithm relies on accurate robot orientation data, which may drift over time as it is derived from proprioceptive odometry sensors. Therefore, the current robot position

Fig. 2. Mobile robot platform with 4×2 antenna array that drives in the corridor and is tracked by a Leica TS30 tachymeter.

Fig. 3. Open-plan office with RFID tags attached to seven privacy walls. The door to the adjoining corridor can be seen on the lower-left side of the image.
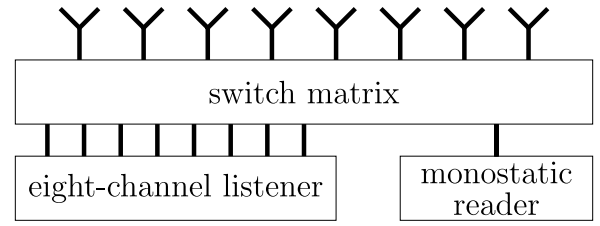

Fig. 4. Block diagram of the robot setup, consisting of eight antennas, a switch matrix, the eight-channel listener [11], and the monostatic reader (Sirit Infinity 610).
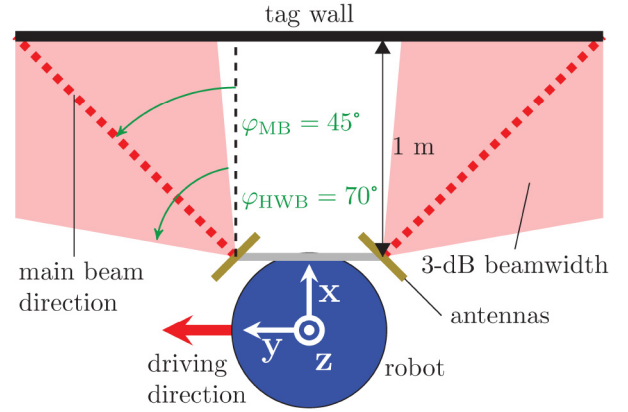

Fig. 5. Radiating geometry of the antenna array with the visualization of the main beam directions and the 3 dB beamwidth. Furthermore, the robot-related coordinate system is defined.

can only be roughly determined using uncorrected odometry data. The application of proprioceptive data corrected for the estimated offsets remarkably increases the accuracy of the determined antenna positions in the subsequent period, resulting in an improved estimate of the mobile robot's position. By continuously updating the odometry offsets, the corrected odometry data successively approximate the true robot positions.

III. SYSTEM ARCHITECTURE

This section describes the UHF RFID mobile robot platform and the measurement scenario used to evaluate the proposed robot self-localization algorithm. The measurement setup is shown in Figs. 2 and 3.

A. UHF RFID Mobile Robot Platform

To communicate with the UHF RFID tags and thus extract the tag ID and phase information from the received tag response, the mobile robot platform is equipped with the custom eight-channel UHF RFID system developed in [11]. A block diagram of the hardware setup is depicted in Fig. 4. This setup consists of a commercial off-the-shelf (COTS) monostatic reader (Sirit Infinity 610 [41]) and an eight-channel UHF

RFID listener, both of which are connected to a switch matrix. The reader communicates with the tags according to the EPC protocol [2] using a monostatic setup with a single TX/RX antenna. The switch matrix selects this antenna by linking one of the eight antennas to the reader and simultaneously connecting the remaining seven antennas, now working solely as RX antennas, to the listener. Thus, during the measurement, all antennas can temporarily transmit or receive signals, depending on the switch matrix settings. The eight-channel listener extracts the tag ID and the signal phase from all detected tag responses. Unlike most COTS devices, the listener is able to determine phase values with 360° (instead of 180°) phase uniqueness, resulting in twice the range uniqueness.

To describe the positions of the TX and RX antennas, we define a robot-related, right-handed coordinate system. As shown in Fig. 5, the y-axis of this coordinate system is aligned with the driving direction, the z-axis represents the height dimension, and the center of the coordinate system is located at the rotation center of the robot platform. The antennas are attached to the robot in a 4×2-array, with the exact antenna positions given in Table I. As depicted in Figs. 2 and 5, the antenna radiation direction vectors and the x-axis enclose angles of $\varphi_{MB} = \pm 45°$. The antenna has an antenna gain of $8.5\,dBi$ and a $3\,dB$-antenna beamwidth of approximately $\varphi_{HWB} = 70°$, as visualized by the simulated antenna radiation pattern in Fig. 6. Considering the geometric dimensions from Fig. 5 and assuming a minimum distance of $1\,m$ between the robot and the wall where the tags are attached,

TABLE I
ANTENNA POSITIONS

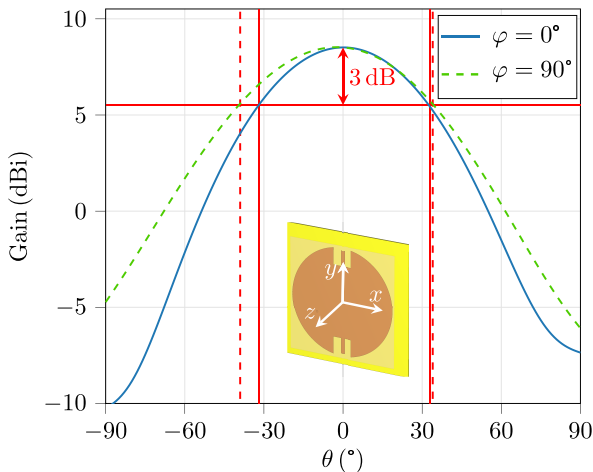| Antenna Index	x (mm)	y (mm)	z (mm)
1	135	157	1668
2	134	-175	1813
3	139	160	1383
4	136	-174	1531
5	138	164	1114
6	139	-173	1247
7	138	168	839
8	140	-171	963

Fig. 6. Antenna radiation patterns at $\varphi = 0°$ and $\varphi = 90°$ as a function of θ. The 3 dB antenna beamwidth is approximately $\varphi_{\mathrm{HWB}} = 70°$, and the antenna gain is 8.5 dBi.

the read range in the y-direction is 11 m. This enables localization, even in harsh environments, where tags can only be placed far apart from each other (e.g., in buildings with obstacles or factory halls with only a few mounting options). The angular resolution of the localization results is indirectly proportional to the largest possible distance between two tags simultaneously detected by a single antenna of the mobile robot platform. Therefore, the conducted optimization of the read range additionally improves the accuracy of the angular estimates, ensuring excellent localization performance.

Moreover, the antenna setup was designed with special care taken to apply a clutter- and multipath-suppressing geometry. Given that the walls of the environment are flat with respect to the carrier wavelength λ_{c}, perpendicular waves are reflected back in the direction of incidence and therefore considerably interfere with the received tag responses, whereas non-perpendicular waves are reflected away from the receiving antennas. The antenna setup mitigates the clutter by attenuating perpendicular waves when moving parallel to the wall, as shown in Fig. 5. Furthermore, the leverage of the multipath effect is reduced by taking advantage of circular antenna polarization [20] and exploiting the spatial diversity of the MIMO architecture. The signal phases of a tag response that was recorded using different MIMO channels (TX-RX antenna combinations) superimpose coherently, whereas multipath components are incoherent because of the

strongly differing signal paths of these channels, which mutually extinguish each other. On the condition that the two antenna array columns are isolated from each other, implementing the switching of the TX antenna increases the number of MIMO channels from 6 to 24, thus strongly contributing to the multipath robustness of the localization system.

The orientation of the robot, which is required to calculate the antenna positions in (1), is estimated internally by evaluating the wheel rotation.

B. Measurement Scenario

The localization algorithm is evaluated in a typical office environment where harsh multipath effects occur. This environment consists of a long corridor and an open-plan office, as shown in Figs. 2 and 3. Fig. 7 depicts a map of the measurement environment that was generated by a laser sensor integrated into the mobile robot platform. This measurement setup enables the everyday suitability of the presented localization algorithm to be proven. The corridor has a width of 2 m and comprises two orthogonal hallways with lengths of 16 m and 31 m. To maintain continuous tag detection, we randomly placed 40 tags on the walls of the corridor.

The open-plan office adjoining to the corridor covers an area of approximately 7 m × 9 m and includes several chairs, tables, and pieces of office equipment. Privacy walls equipped with tags are set up on top of the tables, depicting a realistic office environment and offering the option to distribute the tags over a large area.

During the measurement process, the robot drives through the corridor into the office area. As the driving direction is predefined and the tag detection range is limited to the right side of the robot, the RFID tags in the corridor and in the open-plan office are exclusively placed on the right side of the driveway. Attaching tags on both sides of the wall would allow the robot to drive in both directions. To evaluate the performance of this novel algorithm, the position of the robot is tracked continuously using the optical tracking system Leica TS30, with an accuracy of 3 mm [42].

IV. SIMULATIONS

This section describes a realistic simulation setup to test the developed localization algorithm based solely on RFID data in terms of accuracy and real-time capability. To achieve the most realistic results, the room geometry and the tag and antenna positions from the real measurement are used, whereas the robot positions are calculated by assuming ideal trajectory sections, such as straight lines or circular movements. Considering these simulation parameters, the ideal signal phases detected by the robot-mounted RFID system are calculated according to (3). These ideal phase values differ from the measured values, mainly because of two effects: white phase noise caused by the receiver hardware and multipath propagation. As the standard deviation of the listener's white phase noise (averaged over 10, 000 samples) is $\sigma_\varphi = 0.017$ rad, outperforming COTS devices with typical deviations near $\sigma_\varphi = 0.1$ rad many times over, the phase noise affects the signal phase considerably less compared with the impact of multipath propagation. Thus,
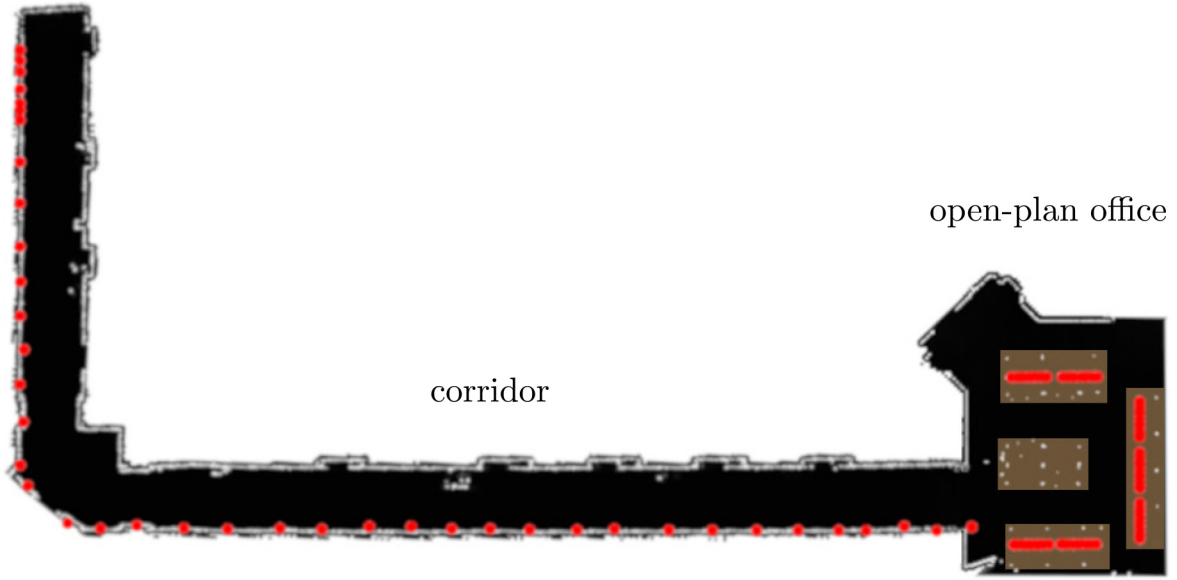
Fig. 7. Laser-generated map of the measurement environment, with the corridor on the left and the open-plan office on the right. The tables are represented by brown rectangles, and the tag positions are marked in red.

this effect is neglected in the following simulation evaluations. Considering multipath propagation, realistic phase values are calculated from the ideal phases by applying the algorithm presented in [43]. To simulate various measurement environments, the factor K (which describes the ratio of the signal power propagating on the line of sight between tag and antenna to the mean multipath signal power) is defined as

$$K = \frac{\text{signal power}}{\text{mean multipath signal power}}. \tag{26}$$

In the simulation, a typical value for indoor environments of $K = 10\,\text{dB}$ is applied.

A decisive variable for comprehending the functionality of the filter and retracing possible filter divergences is the state covariance matrix, which indicates the reliability of the determined localization result. Covariance ellipses are used to graphically visualize the state covariances of the robot positions. These ellipses mark the area around the current filter positions where the deviation is smaller than 20σ, with the filter standard deviation σ calculated from the current state covariance matrix. Thus, a large dimension of the ellipsis along a given direction indicates high state variance in this direction.

Fig. 8 shows the simulated localization results with $\sigma_\varphi = 0\,\text{rad}$ and $K = 10\,\text{dB}$. As the localization error is small, the green plot (visualizing the filter output) completely covers the pink line that depicts the true robot position. All filters are initialized with the same state covariance in the x-direction and the y-direction, leading to a circular covariance ellipsis at the start of the driveway, as shown at $(2\,\text{m}|13\,\text{m})$ in Fig. 8. Given that the position estimation along the antenna–tag direction is directly linked to the measured phase by (3), the localization in this range direction is ambiguous but highly accurate. After the subsequent evaluation of the initial measurement data, this leads to a strong decrease in the state covariance in the range direction and thus deforms the former circular

covariance ellipsis to a more elliptical shape, as shown at $(2\,\text{m}|9\,\text{m})$. Because of the antenna configuration presented in Section III-A, the range vector and the vector pointing in the driving direction enclose angles of $45°$ and $135°$, respectively, explaining the oblique ellipsis orientation. Subsequently evaluating measurements originating from antennas in the other column of the antenna array reduces the state covariance along the major semi-axis of the ellipsis. Hence, the evaluation of measurements from alternating array columns decreases state covariance and transforms the covariance ellipses back into a circular shape. Consecutive bad readings temporarily increase state covariance and deform the covariance ellipses, to be observed at $(23\,\text{m}|0\,\text{m})$. Finally, the robot halts at $(33\,\text{m}|2\,\text{m})$. As the system model assumes that the robot is moving smoothly at a constant speed, stopping causes a deviation between the prediction and the measurement, thus increasing the residuum. The resulting state covariance increment can be observed in the expanding covariance ellipsis. Furthermore, most of the measurement data are recorded by antennas in the rear array column because of the missing tags in front of the robot. This increases the eccentricity of the covariance ellipsis, the semi-minor axis of which is now pointing in the range direction at $\vec{v}_{\text{range}} = (1, 1)^\mathsf{T}$.

Fig. 9 shows the localization error $\Delta r_{t_i} = |\hat{\vec{r}}_{t_i} - \vec{r}_{t_i}|$ as a function of time in blue, with the true robot position $\vec{r}_{t_i}$ and the filter estimate $\hat{\vec{r}}_{t_i}$ at time stamp t_i, and the number of currently initialized filters in red. This number continuously decreases from 15 filters initialized at $t = 0\,\text{s}$, until only one filter remains at $t = 130\,\text{s}$. Because of the low localization error, no filter reinitialization is required during the complete localization process. Shortly after filter initialization, the localization error is larger than $10\,\text{cm}$ because the algorithm is unable to accurately estimate the correct start position due to the multimodal probability density, as described in Section II-D2. By initiating several filters at the most probable start positions
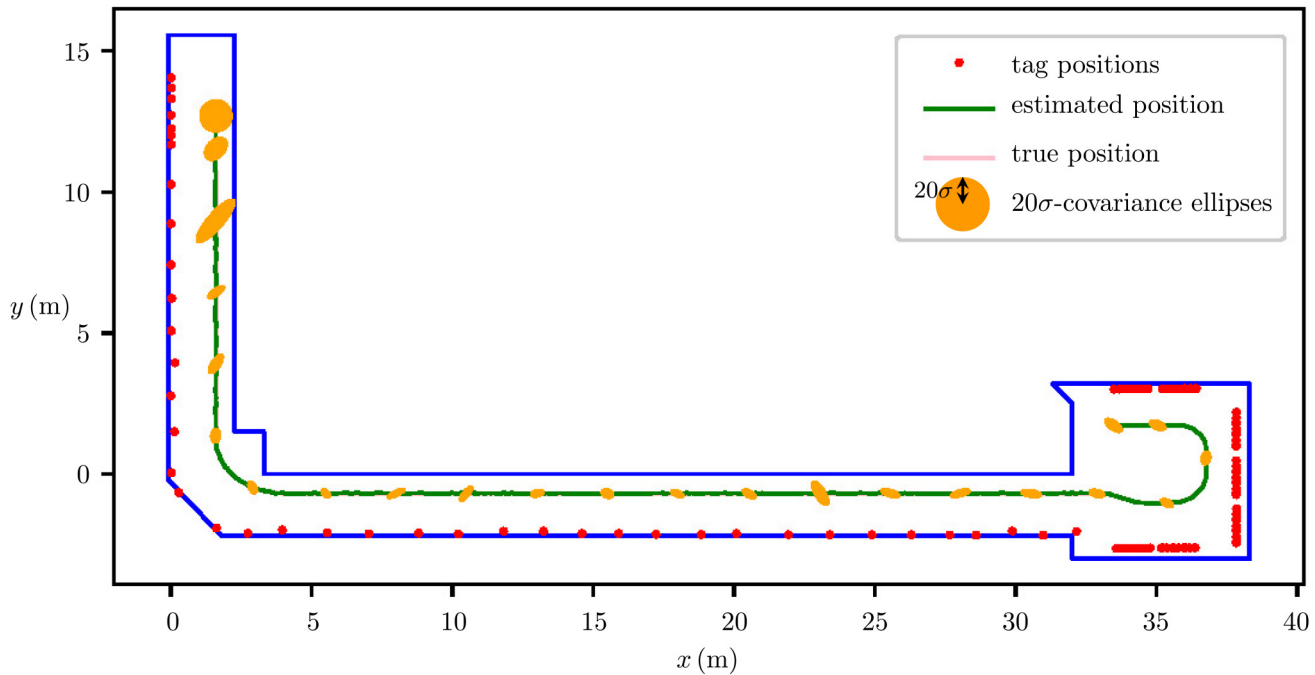
Fig. 8. Simulated localization results (with $\sigma_\varphi = 0$ rad and $K = 10$ dB) plotted on a 2D map of the measuring environment. The estimated position (green) nearly coincides with the true position (pink). The yellow covariance ellipses visualize the continuously decreasing state covariance.
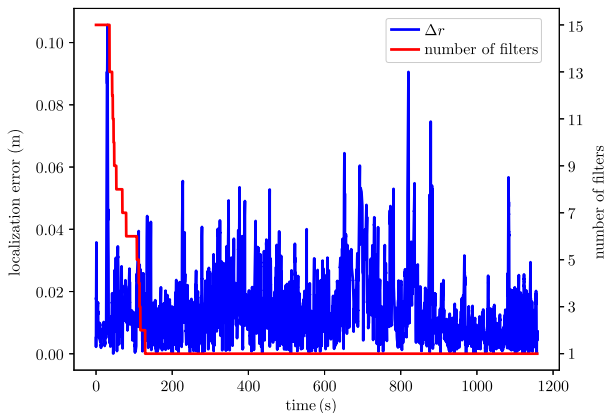

Fig. 9. Simulated localization error and number of initialized filters as a function of time t in s. The number of filters continuously decreases after the initialization at $t = 0$, no reinitialization of filters is required because of the low localization error. The overall RMSE is 1.8 cm.
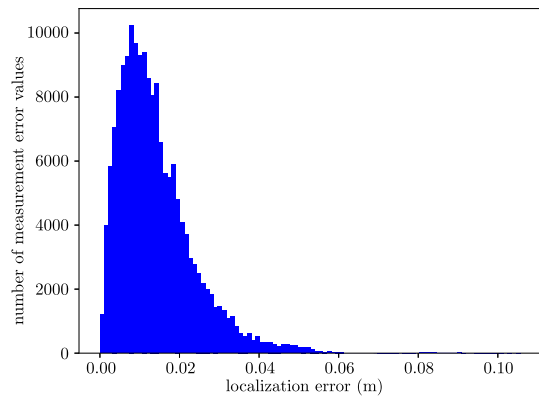

Fig. 10. Histogram of the simulated localization error. Most of the time, the error lies between 0 and 6 cm and exceeds 10 cm only during the initialization phase. The frequency distribution reaches a maximum at an error of approximately 1 cm and then decreases steeply, indicating a low probability of large errors occurring.

and weighing them according to the residuum of prediction and measurement, the error is subsequently limited to 9 cm. Fig. 10 shows a histogram of the simulated localization error. It illustrates that the error lies mainly between 0 and 6 cm, and the frequency distribution reaches a maximum at an error of approximately 1 cm. The overall RMSE of 1.8 cm with

$$\text{RMSE}(\Delta r) = \sqrt{\frac{1}{t_I - t_0} \sum_{i=0}^{I-1} \left[\Delta r_{t_i}^2 (t_{i+1} - t_i) \right]} \qquad (27)$$

validates the outstanding performance of the proposed localization algorithm.

V. MEASUREMENTS

In this section, the hybrid localization algorithm fusing RFID localization results with the odometry data provided by the robot platform is applied to real measurement data. As we use the realistic versatile measurement environment from Section III, the results are generally valid and can be transferred to numerous application scenarios.

As one of the two main components of the hybrid approach, Section V-A shows the results of an RFID-based localization approach, verifying the filter performance that was demonstrated with simulation data in Section IV. This localization approach exclusively evaluates RFID phase measurements and uses the orientation information of the robot's odometry data
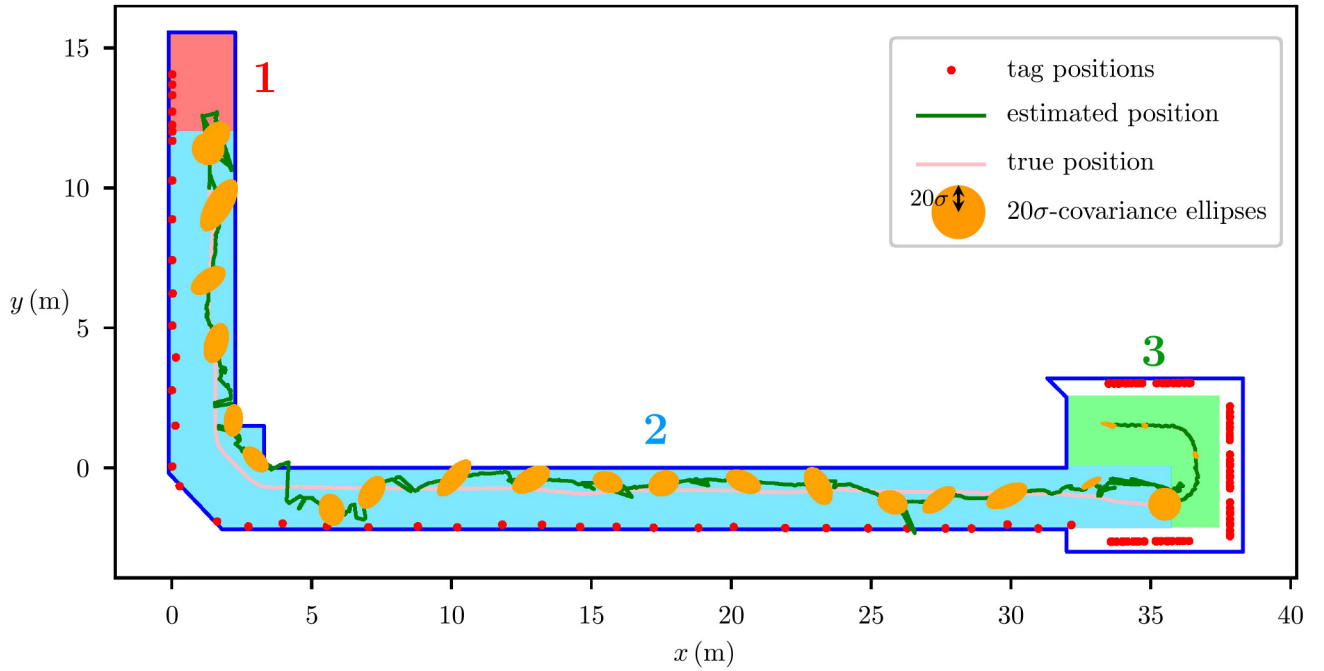
Fig. 11. 2D map of the measured localization results obtained with UHF RFID data only. Because of multipath effects, the estimated position (green) in the hallway strongly deviates from the actual position (pink), resulting in an RMSE of 54.7 cm in Areas 1 and 2. This necessitates a new hybrid approach fusing RFID and odometry data. Given that multipath propagation is much weaker in the open-plan office, the localization error decreases to 4.5 cm in Area 3 once a sufficient amount of undistorted data is recorded, and the shrinking covariance ellipses indicate the growing reliability of the estimated robot position.

solely to compute the antenna positions in (1). Given that the RFID-based localization technique only achieves centimeter precision in environments with weak multipath propagation, Section V-B presents a novel hybrid localization approach utilizing RFID position estimation and erroneous odometry data to accurately determine and subsequently compensate for the robot's odometry deviations.

A. Localization Results Evaluating Only RFID Measurements

Prior to measurement, the localization system must be calibrated to compensate for phase shifts caused by the antennas, cables, switch matrix, and listener. Therefore, the mobile robot platform passes several tags with indices k and measures the phases of the tag responses $\varphi_{\mathrm{mes},k,i,u}$ at time stamps t_i for every single MIMO path u while being tracked by the optical tracking system. Knowing the exact positions of the tags and the mobile robot platform, hypothetical phase values $\varphi_{\mathrm{hyp},k,i,u}$ can be calculated using (3) with $\varphi_{\mathrm{offset},u} = 0$. Subsequently, the phase offset of a given MIMO channel is determined by

$$\varphi_{\mathrm{offset},u} = \arg\left[\sum_{k=0}^{K}\sum_{i=0}^{I} e^{j(\varphi_{\mathrm{mes},k,i,u}-\varphi_{\mathrm{hyp},k,i,u})}\right]. \tag{28}$$

Finally, the calibrated phase of the u-th MIMO-channel is

$$\varphi'_{\mathrm{mes},k,u} = \varphi_{\mathrm{mes},k,i,u} - \varphi_{\mathrm{offset},u}. \tag{29}$$

Given that varying multipath interference is expected in the hallway and the open-plan office because of differing room geometries, adaptive measurement variance is implemented to take the tag position into account during the evaluation of (16), thus adapting the filter parameters to the existing multipath.

Fig. 11 shows the localization results plotted on a 2D map, whereas the localization error and the number of currently initialized filters are given in Fig. 12. Both figures are divided into three sections representing the initialization area, the environment influenced by the hallway, and the open-plan office. The measurement data recorded in the hallway are severely distorted by the multipath effect, which is considerably stronger than assumed in Section IV. Despite the erroneous data leading to high localization error, the filter does not diverge and is therefore capable of continuously providing a rough position estimate with an RMSE of 54.7 cm in Areas 1 and 2. The filter divergence is prevented by applying a new approach that comprises a post-initialization process and a reinitialization process, as described in Section II-D2. In the post-initialization process, five new filters are initialized in the area around the latest position estimate as soon as the filter residual increases sharply, indicating a recent filter deviation. This process, which can be observed several times in Area 2 of Fig. 12, maintains the number of initialized filters within a range of approximately three to nine, so that enough filters are around the true robot position to react quickly to filter deviations. If all filters are deleted because of permanently high filter residuals, a reinitialization process is performed. Therefore, the localization algorithm uses the latest measurement data to determine the current robot position and initializes new filters at the 15 most likely estimates. Fig. 12 visualizes reinitialization at $t = 950\,\mathrm{s}$, which (in combination with hardly distorted measurement data received in the open-plan office) forms the basis for the following highly accurate localization results. From $t = 950\,\mathrm{s}$ onwards, the initialization of new filters is not needed because of the small localization error, leaving only one filter
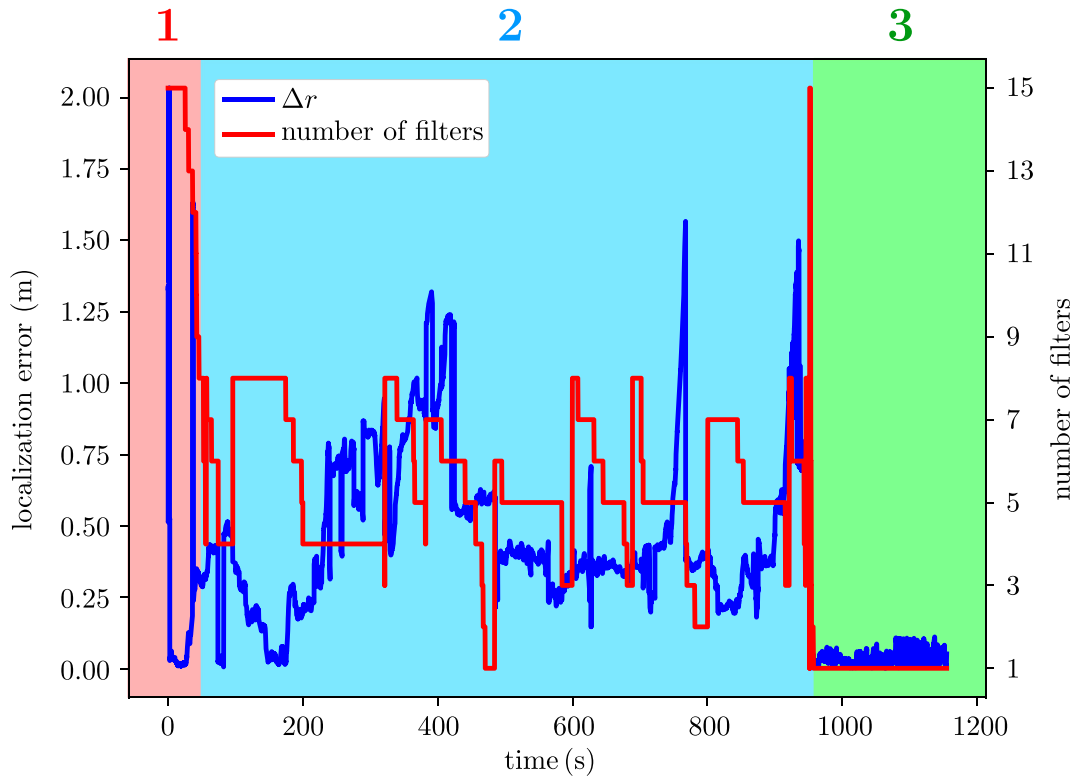
Fig. 12. Measured localization error and number of initialized filters as a function of time t in s when evaluating UHF RFID data only. Because of the strong multipath effect in the hallway, the post-initialization process maintains the number of initialized filters within a range of three to nine in Area 2. Once the robot reaches the open-plan office and has acquired sufficient undistorted data, only one filter remains (located approximately at the true robot position), and the localization error decreases sharply from an RMSE of 54.7 cm in Areas 1 and 2 to 4.5 cm in Area 3.
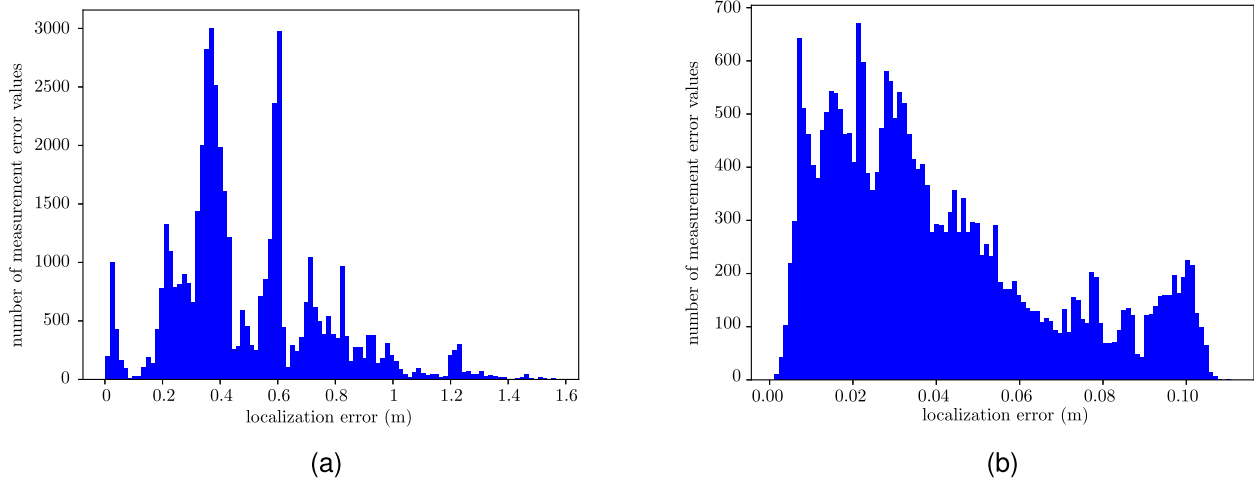

Fig. 13. Histograms illustrating the measured localization errors of Area 2 in (a) and Area 3 in (b). Because of the harsh multipath environment in Area 2, the localization shows large errors in a range between 0 and 160 cm, whereas the mitigated multipath effect in Area 3 leads to a reduced localization error that does not exceed a maximum value of 11 cm.

located at the true position of the mobile robot platform. Moreover, the decrease in the covariance of the filter state, visualized as shrinking covariance ellipses in Fig. 11, indicates the growing reliability of the estimated robot position. In Area 3, the localization algorithm estimates the position of the mobile robot platform with an accuracy of 4.6 cm RMSE. The localization error slightly increases at $t = 1100$ s because the stopping of the robot deviates from the system model, which assumes uniform robot motion, as described in Section IV.

Fig. 13 shows two histograms illustrating the measured localization errors of Areas 2 and 3. Similar to the simulated error in Fig. 10, the frequency distribution of Area 3 in Fig. 13(b) decreases steeply toward high error values. Even though the maximum error of the measured localization results is similar to the simulated error, the lower slope of the frequency distribution decrease toward high error values and the shift of the maximum, which is now at 2 cm, result in an increased RMSE of 4.6 cm compared with the simulated value of 1.8 cm.
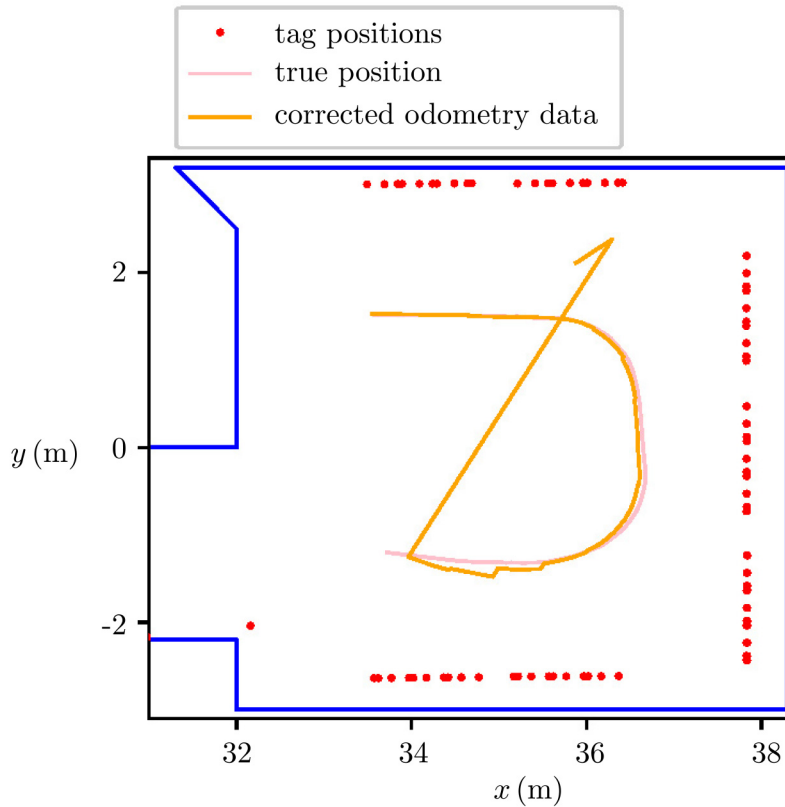
Fig. 14. True robot position in pink and successively corrected odometry data in yellow. By determining the position and orientation offset of the odometry data using the RFID-based localization results of the open-plan office, the algorithm can estimate the robot position with an RMSE of 2.7 cm.

Because of the harsh multipath environment in Area 2, the localization error reaches up to 160 cm, as shown in Fig. 13(a). The frequency distribution has two maxima at 4 and 6 cm, which result from the localization intervals [500 s, 900 s] and [200 s, 500 s], respectively, as shown in Fig. 12

B. Compensation for the Proprioceptive Drift by Data Fusion

Although the presented RFID-based localization algorithm successfully prevents filter divergence, even in environments with severe multipath distortions, a coarse position estimation with an RMSE of 54.7 cm in Areas 1 and 2 (see Figs. 11 and 12) does not meet the requirements for most applications. To compensate for the drift error of odometry and ensure sustained high localization accuracy even in harsh multipath environments, we applied the data fusion approach described in Section II-E, fusing exteroceptive RFID localization results with faulty odometry data. Fig. 14 shows the process of odometry correction applied to the measurement data of the open-plan office. To demonstrate the outstanding performance of the algorithm, we chose exceptionally high initial odometry errors of $\Delta x = 2.2$ m, $\Delta y = 3.3$ m, and $\Delta \phi = 40°$. The true robot position (determined using the optical tracking system) is shown in pink, whereas the yellow line represents the corrected odometry data. The position and orientation errors are estimated every 10 s, causing the corrected odometry data to converge quickly from the high initial offset to the true robot
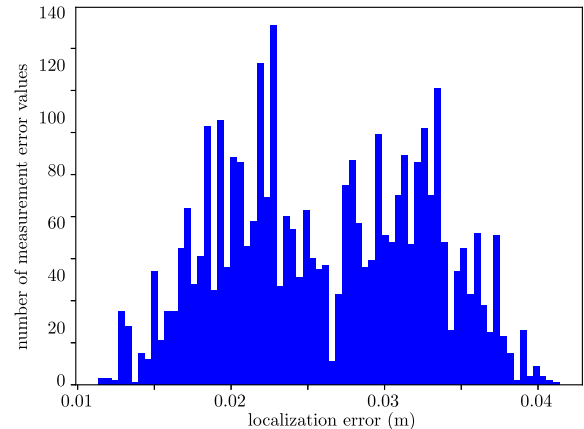

Fig. 15. Histogram of the localization error from (36.4 m|1.0 m) to the end of the track using the hybrid localization approach. Similar to that in Fig. 13(b), the maximum of the frequency distribution is between 2 and 3 cm, whereas the maximum localization error is reduced to 4 cm by fusing the RFID localization results with the odometry data.

positions. When passing (36.4 m|1.0 m), the algorithm accurately estimates the odometry offset, reducing the RMSE to 2.7 cm. Fig. 15 shows a histogram of the localization error measured in this last section of the track. Comparing this result with the error of the RFID-based localization approach in Fig. 13(b), we see that the maximum of the frequency distribution is still at $2 - 3$ cm, but the number of large errors is considerably reduced by fusing the RFID-based results with

odometry data. Thus, the maximum localization error is now only 4 cm, corresponding to a reduction of approximately 60 %.

The fusion of odometry data with RFID localization results not only remarkably improves the accuracy of the robot position estimation in a mild multipath environment but also enables high-precision localization under conditions where RFID localization is barely possible, so long as the robot regularly traverses light multipath surroundings to compensate for odometry drift.

VI. Conclusion

In this paper, we presented a localization algorithm that estimates the location of a mobile robotic platform by evaluating the phase information and transponder IDs of UHF RFID tag responses and fusing the resulting position estimates with the robot's odometry data. By running multiple UKFs and successively deleting the filters with the least reliable position estimations, the multihypothesis approach resolves the position ambiguity caused by the 2π-phase ambiguity of the tag responses. The localization algorithm based solely on RFID data was validated, and the behavior of the state covariances was reproduced using a realistic simulation environment and reasonable choices for the expected multipath. Testing this system in a realistic office environment demonstrated that the algorithm can estimate the location of the robot with an RMSE of 4.6 cm in a region with weak multipath distortions. However, in harsh environments, the algorithm provides only coarse position estimates with an RMSE of 54.7 cm, necessitating the fusion of RFID localization results and odometry data from the robot.

Therefore, a novel hybrid approach was presented, combining RFID localization with the robot's odometry data to estimate odometry offsets, even in the presence of high initial error, thus compensating for odometry drift. This reduces the RMSE to 2.7 cm in the open-plan office and enables permanent, high-precision localization without the need for expensive exteroceptive sensors, such as camera, sonar, or laser technologies.

In future research, the required tag density can be reduced using active transponders that increase the reading range of the RFID system by transmitting amplified tag responses. This can enable high-precision localization in environments with few mounting positions and thus large antenna–tag distances, such as factory buildings or warehouses.

Acknowledgment

References

[1] "Professionelle Mobile Service-Roboter—MetraLabs." [Online]. Available: https://www.metralabs.com/ (Accessed: Feb. 7, 2022).

[2] *Class-1 Generation-2 UHF RFID Protocol for Communications at 860 MHz–960 MHz, Version 1.2.0 Ed.*, EPC Global, Brussels, Belgium, Oct. 2008.

[3] "RFID market with COVID-19 impact analysis by product type (tags, readers, and software and services), wafer size, tag type (passive tags and active tags), frequency, applications, form factor, material, and region—Global forecast to 2026," Res. Markets Ltd., Dublin, Ireland, Rep. 5292847, Feb. 2021. [Online]. Available: https://www.researchandmarkets.com/reports/5292847/rfid-market-with-covid-19-impact-analysis-by

[4] D. M. Dobkin, *The RF in RFID—Passive UHF RFID in Practice*. Burlington, VT, USA: Elsevier, 2008.

[5] A. Motroni, A. Buffi, and P. Nepa, "A survey on indoor vehicle localization through RFID technology," *IEEE Access*, vol. 9, pp. 17921–17942, 2021.

[6] C. Li, L. Mo, and D. Zhang, "Review on UHF RFID localization methods," *IEEE J. Radio Freq. Identif.*, vol. 3, no. 4, pp. 205–215, Dec. 2019.

[7] R. Miesen *et al.*, "Where is the tag?" *IEEE Microw. Mag.*, vol. 12, no. 7, pp. S49–S63, Dec. 2011.

[8] M. Gareis, A. Parr, J. Trabert, T. Mehner, M. Vossiek, and C. Carlowitz, "Stocktaking robots, automatic inventory, and 3D product maps: The smart warehouse enabled by UHF-RFID synthetic aperture localization techniques," *IEEE Microw. Mag.*, vol. 22, no. 3, pp. 57–68, Mar. 2021.

[9] A. Tzitzis *et al.*, "Real-time 3D localization of RFID-tagged products by ground robots and drones with commercial off-the-shelf RFID equipment: Challenges and solutions," in *Proc. IEEE Int. Conf. RFID (RFID)*, Sep. 2020, pp. 1–8.

[10] L. Shangguan, Z. Yang, A. X. Liu, Z. Zhou, and Y. Liu, "STPP: Spatial-temporal phase profiling-based method for relative RFID tag localization," *IEEE/ACM Trans. Netw.*, vol. 25, no. 1, pp. 596–609, Feb. 2017.

[11] M. Gareis *et al.*, "Novel UHF-RFID listener hardware architecture and system concept for a mobile robot based MIMO SAR RFID localization," *IEEE Access*, vol. 9, pp. 497–510, 2021.

[12] C. F. Olson, "Probabilistic self-localization for mobile robots," *IEEE Trans. Robot. Autom.*, vol. 16, no. 1, pp. 55–66, Feb. 2000.

[13] F. Valenti, D. Giaquinto, L. Musto, A. Zinelli, M. Bertozzi, and A. Broggi, "Enabling computer vision-based autonomous navigation for unmanned aerial vehicles in cluttered GPS-denied environments," in *Proc. 21st Int. Conf. Intell. Transp. Syst. (ITSC)*, Nov. 2018, pp. 3886–3891.

[14] S. J. Kim and B. K. Kim, "Dynamic ultrasonic hybrid Localization system for indoor mobile robots," *IEEE Trans. Ind. Electron.*, vol. 60, no. 10, pp. 4562–4573, Oct. 2013.

[15] T. Einsele, "Real-time self-localization in unknown indoor environment using a panorama laser range finder," in *Proc. IEEE/RSJ Int. Conf. Intell. Robot Syst. Innov. Robot. Real-World Appl. (IROS)*, vol. 2, Sep. 1997, pp. 697–702.

[16] P. Vorst and A. Zell, "Fully autonomous trajectory estimation with long-range passive RFID," in *Proc. IEEE Int. Conf. Robot. Autom.*, May 2010, pp. 1867–1872.

[17] S. S. Saab and Z. S. Nakad, "A standalone RFID indoor positioning system using passive tags," *IEEE Trans. Ind. Electron.*, vol. 58, no. 5, pp. 1961–1970, May 2011.

[18] A. Motroni, A. Buffi, P. Nepa, and B. Tellini, "Sensor-fusion and tracking method for indoor vehicles with low-density UHF-RFID tags," *IEEE Trans. Instrum. Meas.*, vol. 70, pp. 1–14, Sep. 2020, doi: 10.1109/TIM.2020.3027926.

[19] A. Motroni, P. Nepa, A. Buffi, and B. Tellini, "Robot localization via passive UHF-RFID technology: State-of-the-art and challenges," in *Proc. IEEE Int. Conf. RFID (RFID)*, Sep. 2020, pp. 1–8.

[20] E. DiGiampaolo and F. Martinelli, "Mobile robot localization using the phase of passive UHF RFID signals," *IEEE Trans. Ind. Electron.*, vol. 61, no. 1, pp. 365–376, Jan. 2014.

[21] F. Martinelli, "A robot localization system combining RSSI and phase shift in UHF-RFID signals," *IEEE Trans. Control Syst. Technol.*, vol. 23, no. 5, pp. 1782–1796, Sep. 2015.

[22] B. Tao, H. Wu, Z. Gong, Z. Yin, and H. Ding, "An RFID-based mobile robot localization method combining phase difference and readability," *IEEE Trans. Autom. Sci. Eng.*, vol. 18, no. 3, pp. 1406–1416, Jul. 2021.

[23] M. Gareis, C. Carlowitz, and M. Vossiek, "A MIMO UHF-RFID SAR 3D locating system for autonomous inventory robots," in *Proc. IEEE MTT-S Int. Conf. Microw. Intell. Mobility (ICMIM)*, Nov. 2020, pp. 1–4.

[24] X. Xuan, L. Lv, and K. Li, "A miniaturized meandered dipole UHF RFID tag antenna for flexible application," *Int. J. Antennas Propag.*, vol. 2016, May 2016, Art. no. 2951659.

[25] I. Frigui, M. S. Karoui, and H. Ghariani, "A study of the bends effects on a meandered dipole tag antenna," in *Proc. 11th Int. Des. Test Symp. (IDT)*, Dec. 2016, pp. 284–289.

[26] N. Beuster *et al.*, "UHF RFID tag response measurements using a do-it-yourself platform and components off-the-shelf," *IEEE J. Radio Freq. Identif.*, vol. 4, no. 1, pp. 65–72, Mar. 2020.

[27] M. Gareis, P. Fenske, C. Carlowitz, and M. Vossiek, "Particle filter-based SAR approach and trajectory optimization for real-time 3D UHF-RFID tag localization," in *Proc. IEEE Int. Conf. RFID (RFID)*, 2020, pp. 1–8.

[28] S. Thrun, W. Burgard, and D. Fox, *Probabilistic Robotics*. Cambridge, MA, USA: MIT Press, 2006.

[29] R. E. Kalman, "A new approach to linear filtering and prediction problems," *J. Basic Eng.*, vol. 82, no. 1, pp. 35–45, Mar. 1960.

[30] S. Challa, M. R. Morelande, D. Mušicki, and R. J. Evans, *Fundamentals of Object Tracking*. Cambridge, U.K.: Cambridge Univ. Press, 2011.

[31] R. Faragher, "Understanding the basis of the Kalman filter via a simple and intuitive derivation [lecture notes]," *IEEE Signal Process. Mag.*, vol. 29, no. 5, pp. 128–132, Sep. 2012.

[32] G. Welch and G. Bishop, "An introduction to the Kalman filter," in *Proc. Siggraph Course*, vol. 8, Jan. 2006, pp. 1–16.

[33] E. A. Wan and R. Van Der Merwe, "The unscented Kalman filter for nonlinear estimation," in *Proc. IEEE Adapt. Syst. Signal Process. Commun. Control Symp.*, 2000, pp. 153–158.

[34] R. Zhan and J. Wan, "Iterated unscented Kalman filter for passive target tracking," *IEEE Trans. Aerosp. Electron. Syst.*, vol. 43, no. 3, pp. 1155–1163, Jul. 2007.

[35] B. M. Bell and F. W. Cathey, "The iterated Kalman filter update as a Gauss–Newton method," *IEEE Trans. Autom. Control*, vol. 38, no. 2, pp. 294–297, Feb. 1993.

[36] Y.-A. Zhang, D. Zhou, and G.-R. Duan, "An adaptive iterated Kalman filter," in *Proc. Multiconf. Comput. Eng. Syst. Appl.*, vol. 2, Oct. 2006, pp. 1727–1730.

[37] M. Li, Z. Chen, and X. Shao, "Iterated unscented Kalman particle filter algorithm based on a variable-step adaptive artificial fish swarm optimization," in *Proc. 35th Chin. Control Conf. (CCC)*, Jul. 2016, pp. 7050–7053.

[38] H. Qian and Z. Qiu, "Iterated unscented Kalman filter for spacecraft attitude estimation," in *Proc. 37th Chin. Control Conf. (CCC)*, Jul. 2018, pp. 4557–4562.

[39] G. Li and H. Yang, "Iterated square root unscented Kalman particle filter," in *Proc. IEEE Youth Conf. Inf., Comput. Telecommun.*, Nov. 2010, pp. 222–225.

[40] K.-H. Kim, J.-H. Song, and G.-I. Jee, "The GPS vector tracking loop based on the iterated unscented unscented Kalman filter under the large initial error," in *Proc. Eur. Control Conf. (ECC)*, Aug. 2009, pp. 3701–3706.

[41] "Users Guide." 2011. [Online]. Available: https://fccid.io/M4ZIN610/User-Manual/User-Manual-1555467 (Accessed: Feb. 17, 2022).

[42] "Leica TS 30 Technical Data." 2009. [Online]. Available: https://leica-geosystems.com/SFTP/files/archived-files/TS30_Technical_Data_en.pdf (Accessed: Feb. 17, 2022).

[43] A. Parr, R. Miesen, and M. Vossiek, "Comparison of phase-based 3D near-field source localization techniques for UHF RFID," *Sensors*, vol. 16, no. 7, p. 978, Jul. 2016.

Tobias Kögel (Graduate Student Member, IEEE) was born in Lauf, Germany, in 1995. He received the M.Sc. in electrical engineering from Friedrich-Alexander-Universität Erlangen-Nürnberg (FAU), Erlangen, Germany, in 2020, where he is currently pursuing the Ph.D. degree with the Institute of Microwaves and Photonics. His current research interests include radar and localization systems for indoor environments based on UHF RFID technology.

Matthias Gareis was born in Kronach, Germany, in 1992. He received the M.Sc. degree in electrical engineering and the Dr.-Ing. degree from Friedrich-Alexander-University Erlangen-Nürnberg, Erlangen, Germany, in 2016 and May 2021, respectively. Since January 2021, he has been working with Rohde & Schwarz in the area of microwave imaging.

Christoph Kammel was born in Nuremberg, Germany, in 1996. He received the M.Sc. degree in electrical engineering from Friedrich-Alexander-University Erlangen-Nürnberg (FAU), Erlangen, Germany, in 2020, where he is currently pursuing the Ph.D. degree with the Institute of Microwaves and Photonics. His current research interests include radar imaging and signal processing in the space sector.

Martin Vossiek (Fellow, IEEE) received the Ph.D. degree from Ruhr-Universität Bochum, Bochum, Germany, in 1996. In 1996, he joined Siemens Corporate Technology, Munich, Germany, where he was the Head of the Microwave Systems Group from 2000 to 2003. Since 2003, he has been a Full Professor with Clausthal University, Clausthal-Zellerfeld, Germany. Since 2011, he has been the Chair with the Institute of Microwaves and Photonics, Friedrich-Alexander-Universität Erlangen-Nürnberg, Erlangen, Germany.

He has authored or coauthored more than 300 articles. His research has led to nearly 100 granted patents. His current research interests include radar, transponder, RF identification, communication, and wireless locating systems. He received more than 10 best paper prizes and several other awards. For example, he was awarded the 2019 Microwave Application Award from the IEEE MTT Society (MTT-S) for Pioneering Research in Wireless Local Positioning Systems. He serves on the advisory board of the IEEE CRFID Technical Committee on Motion Capture & Localization. He is a member of the German National Academy of Science and Engineering (acatech), the German Research Foundation (DFG) review board, the German IEEE Microwave Theory and Techniques (MTT)/Antennas and Propagation (AP) Chapter Executive Board, the IEEE MTT Technical Committees MTT-24 Microwave/mm-wave Radar, Sensing, and Array Systems; MTT-27 Connected and Autonomous Systems (as founding chair); and MTT-29 Microwave Aerospace Systems. He has been a member of organizing committees and technical program committees for many international conferences, and he has served on the review boards of numerous technical journals. From 2013 to 2019, he was an Associate Editor for the IEEE TRANSACTIONS ON MICROWAVE THEORY AND TECHNIQUES.